Journal of Zhejiang University-SCIENCE A 2026 27(7):676-695
www.jzus.zju.edu.cn; www.springer.com/journal/11582
E-mail: jzus_a@zju.edu.cn

Research Article
https://doi.org/10.1631/jzus.A2500549

Check for updates

Adaptive adjustment strategy for earth pressure balance (EPB) operation parameters for pre-control of shield tunneling-induced surface settlement: a case study

Dongsheng WEI, Haibin WEI, Zipeng MA✉, Heting WEI, Lijie SUN, Xiaokun YU

College of Transportation, Jilin University, Changchun 130000, China

Abstract: During shield tunneling, ground deformation poses significant safety risks. The full optimization strategy ignores interactions between parameters, resulting in suboptimal performance in the pre-control of settlement in earth pressure balance shields. To address this problem, this paper proposes an integrated strategy that combines optimization and inversion, minimizing parameter interaction interference through adaptive adjustment of shield operation parameters. This mechanism performs an optimization search on the key operation parameters for settlement control, while the remaining operation parameters are predicted through inversion. Taking the Changchun Metro Line 6 project as an example, a bidirectional long short-term memory (Bi-LSTM) model enhanced by a multi-head self-attention (MHSA) mechanism is used to predict shield tunneling-induced settlement with spatiotemporal sequence dependency relationships. Particle swarm optimization and a random forest algorithm are used for optimization and inversion operations in the integrated mechanism, respectively. Subsequent ring position tests showed that the integrated mechanism-based adaptive adjustment strategy limited the average fluctuation of uncontrollable parameters to ±13.95% compared to ±34.27% for the full optimization strategy. The actual average settlement was only 3.81 mm compared to 4.72 mm for the full optimization strategy through collaborative parameter adjustment. The application validated the feasibility and applicability of the integrated mechanism, providing important references for the adaptive adjustment of shield parameters and tunnel construction automation.

Key words: Pre-control of settlement; Optimization and inversion; Multi-head self-attention (MHSA); Long short-term memory (LSTM); Random forest (RF) algorithm

1 Introduction

The development of underground space effectively addresses the challenges associated with urban sprawl, with subway-led underground rail systems rapidly advancing (Xu and Chen, 2023). Shield tunneling, favored for its minimal disruption, efficiency, and cost-effectiveness, is extensively utilized in underground construction projects (Hou et al., 2022). However, the process presents risks such as groundwater influx and geological hazards, which are particularly concerning when tunneling near existing structures. Excessive settlement in these areas can damage buildings and underground utilities, significantly threatening public safety and property. Given these risks, controlling settlement during shield tunneling has become an urgent issue in current underground transportation construction, requiring the adoption of effective measures to limit surface settlements.

At present, conventional technical methods for controlling shield tunneling-induced surface settlement mainly involve adjusting shield operation parameters and grouting treatment inside and outside the tunnel based on on-site measured settlement data. However, the passive remediation measures taken after settlement exhibit hysteresis, potentially causing irreversible residual deformations, and thereby posing safety risks to the utilization and functionality of sensitive buildings and structures. To predict settlements caused by shield tunneling, a multitude of researchers have engaged in pertinent studies utilizing methods such as empirical formulas (Mair et al., 1993; Standing and

✉ Zipeng MA, mazp@jlu.edu.cn
Dongsheng WEI, https://orcid.org/0000-0003-0789-4249

Received Oct. 28, 2025; Revision accepted Apr. 22, 2026; Crosschecked May 31, 2026; Online first June 27, 2026

Burland, 2006; Luo et al., 2020; Zhang YQ et al., 2021), analytical solutions and in situ predictions (Galera et al., 2007; Deng and Wang, 2013), and numerical simulations (Maleki, 2018; Zhang et al., 2020a). Concurrently, various strategies for estimating the optimal operation parameters of shield tunneling have been proposed. Due to the spatial variability of geological and geotechnical parameters, estimates based on empirical and analytical formulas are often not accurate enough, and numerical methods, which are time-consuming in model creation and computation, are not very feasible in the optimization of shield parameters that have strong real-time requirements.

With the development of computer science, digital twins, big data analysis, and other technologies continue to develop and integrate increasingly closely in various industries (Hu et al., 2025). The innovative thinking of industrial integration has led to significant achievements in various fields. In civil engineering intelligent construction (CEIC), machine learning (ML) methods can find the mathematical relationship between various factors and the predicted target in a data-driven way and can obtain the predicted result in a short time, which makes ML play an important role in the field of surface settlement prediction caused by shield tunneling (Suwansawat and Einstein, 2006; Chen et al., 2022; Kong et al., 2022). When using an artificial neural network (ANN), a backpropagation neural network (BPNN) has been applied for the first time to predict surface settlement, which is acceptable despite the prediction error (Kim et al., 2001). To reduce the prediction error and minimize the risk of tunneling, Pourtaghi and Lotfollahi-Yaghin (2012) proposed an alternative method for predicting the maximum surface settlement based on the integration of wavelet theory and ANN. Currently, an increasing number of ML methods have been adopted, such as decision tree (DT), Lasso regression, support vector regression (SVR) (Wei et al., 2023), random forest (RF) (Zhang et al., 2020c), and gradient boosting decision tree (GBDT) (Zhang WG et al., 2021; Zhou ZX et al., 2023). Additionally, more scholars have combined ML with optimization algorithms to reduce errors in settlement prediction by reasonably optimizing models or processing variables (Shi et al., 2021; Zhou Z et al., 2023). It has been found that long short-term memory (LSTM) has stronger memory retention and selection ability (Zhang et al., 2020b; Li et al., 2022; Al Mehedi et al., 2023) and can consider the sequence effects of deformation and surface settlement caused by shield tunneling. Attention mechanisms, introduced in recent years, excel at learning spatiotemporal correlations between datasets by assigning attention weights to individual steps, demonstrating an outstanding ability to capture long-term dependencies between steps, key data information, and internal autocorrelations within the data. LSTM variants, e.g., CNN-SA-LSTM (Gao et al., 2024; Yang et al., 2025) and CNN-LSTM-Attention (Zhao et al., 2024; Bao et al., 2025; Wang et al., 2025), incorporate a self-attention (SA) mechanism and a convolutional neural network (CNN), demonstrating significantly higher accuracy and handling sequential data well. Although the multi-head self-attention (MHSA) mechanism is more effective than the SA mechanism in extracting richer data features from a multilevel perspective across various subspaces, there is limited research on integrating it within existing models to predict surface settlement caused by shield tunneling (Song et al., 2024). Therefore, in this study, the bidirectional LSTM (Bi-LSTM) model was selected as the baseline framework and integrated with the MHSA mechanism to form the MHSA-Bi-LSTM model to capture spatiotemporal correlations and extract key data features.

In practical engineering, the control of shield tunneling parameters mainly relies on manual experience, which is significantly subjective. Improper parameter adjustment has become the main cause of recent shield tunneling accidents. An increasing number of studies have shown that there is a close relationship between geotechnical parameters, tunneling parameters, and settlement deformation in shield construction. Some scholars have carried out in-depth studies on the optimization of tunneling parameters to ensure that the shield can operate efficiently under the expected working conditions. Liu and Ding (2020), through sensitivity analysis, found that synchronous grouting pressure and advance speed are parameters affecting the support pressure, while cutter rotating speed, cutter torque, and actual excavation amount are parameters affecting the deviation angle. Close attention to and adjustment of parameters with greater impact can thus optimize the tunnel excavation process. Lin et al. (2021) established a muck chamber support pressure prediction model based on a genetic algorithm (GA)-BPNN and proposed an optimization mechanism for tunneling parameters, which enables the prediction and control of support pressure. When the control of surface settlement is considered as a separate criterion, researchers (Hou et al., 2020; Sun, 2022) have put forward a similar approach, mainly finding the shield parameters by searching. Although this method can effectively reduce the computational complexity, the synergistic effect between some parameters, such as support pressure and cutter torque, is ignored and is jointly determined by controllable operation parameters as well as geometric and ground conditions, which leads to a discrepancy between theoretical results and actual operation, and thus resulting in a lack of practical engineering value. In response, Zhang et al. (2019) proposed a method for optimizing shield operation parameters when settlement exceeds the allowable value, which involves preventing abnormal settlement through parameter adjustment. This method requires a clear division of superior and inferior subsets of samples, and inevitably, there will be some limitations in its application. Optimizing shield operation parameters to guide the shield work in the best configuration state still requires further in-depth research within the engineering field.

In light of the current state of affairs, this study introduces a mechanism that integrates an optimization and inversion algorithm. It is designed to achieve preemptive management of surface settlement, mitigating the interference of interdependencies among shield parameters. The MHSA-Bi-LSTM and RF methods are applied to the prediction of settlement with sequence relationships and the inversion prediction of operation parameters with limited monitoring accuracy, respectively. A partitioning strategy for operation parameters is proposed, thereby establishing a composite optimization mechanism. A case study is presented, demonstrating the practical implementation and effectiveness of the proposed method from the Changchun Metro Line 6 construction project. The proposed method uses settlement control as a separate judging criterion for constructing a recommendation system of operation parameters to assist shield driving, and therefore promoting advancement in the field of shield automation and reducing construction safety problems.

2 Methodology

2.1 Shield tunneling-induced surface settlement forecast model

Earth pressure balance (EPB) shields turn the excavated material into a soil paste by soil conditioning that is used as a pliable and plastic support medium. This makes it possible to balance the pressure conditions at the tunnel face, avoids uncontrolled inflow of soil into the machine, and creates the conditions for rapid tunneling with minimum settlement (Herrenknecht, 2024). Fig. S1 of the electronic supplementary materials (ESM) shows a comprehensive schematic of key parameters and the shield tunneling process in EPB construction.

Since it is impossible to achieve single-variable control in actual shield tunneling, a unique relationship between surface settlement and various parameters cannot be determined, but the surface settlement is affected by multifactor coupling (Li et al., 2015). In computer simulation or ML studies, the main factors influencing surface settlement are categorized into geometric parameters, geotechnical parameters, and shield operation parameters. The surface settlement caused by shield construction can be regarded as a spatiotemporal sequence prediction problem: the surface settlement at a particular moment (time) and at a particular location (space), for example, at the back of the completed excavation ring (space) (Ding et al., 2013; Richa et al., 2023). The pre-shield arrival surface settlement at a particular time is affected by factors such as the support pressure on the unreached section. Therefore, it is necessary to predict the surface settlement based on multifactor spatial sequence data.

In the context of tunnel engineering, the depth-to-span ratio (the ratio of cover depth to tunnel diameter) and the center-to-center distance of twin tunnels are recognized as critical geometric parameters that substantially influence shield tunneling-induced surface settlement (S_s). However, tunnel dimensions are typically fixed in each individual engineering study. The twin tunnels in this project are nearly parallel, with a center-to-center distance ranging from 13 to 17 m. This distance satisfies the empirical criterion of being greater than 2.0 times the tunnel diameter, which is widely recognized as a reasonable range to minimize interaction effects between adjacent tunnels and ensure construction safety (Ghaboussi and Ranken, 1977; Hage Chehade and Shahrour, 2008). Consequently, the cover depth (D_C) is identified as the only geometric parameter for consideration.

Drawing on pertinent literature (Zhang et al., 2020b; Li et al., 2022), key geotechnical parameters are identified as the constrained modulus (E_{oed}), cohesion (c), angle of internal friction (φ), and lateral earth pressure coefficient at rest (K_0). During soil mechanics property experiments for this engineering project, minimal variations in Poisson's ratio and void ratio (e) of distinct soil strata were observed, suggesting that these parameters have a negligible influence on settlement. Wu et al. (2019) and Huang et al. (2021) have highlighted the presence of groundwater seepage at the excavation face and the interface of the tail shield as contributing to the consolidation settlement of the soil. The altitude of the groundwater table not only indirectly regulates the rate of seepage but also influences the soil stability. Therefore, the water table level (L_W) is selected as an important hydrogeological parameter.

Research has demonstrated that the majority of shield operation parameters, to varying degrees, can influence surface settlement. Nonetheless, an overabundance of input parameters with excessive dimensionality may lead to difficulties in model convergence. Thus, parameters that have direct or indirect interactions with the soil are prioritized. Accordingly, the volume of synchronous grouting (V_G) (Niu et al., 2023), total thrust (T_T), cutterhead torque (T_C), cutterhead rotating speed (R_C) (Wang et al., 2021), support pressure (P_S), advance speed (S_A) (Cheng et al., 2022), screw conveyor rotating speed (R_{SC}), screw conveyor torque (T_{SC}), and volume of excavated earth (V_E) (Lv et al., 2020) are selected as the relevant shield operation parameters. Previous studies have identified that these parameters exert a significant influence on the stability of the excavation face and surface settlement (Hu et al., 2021).

Given the numerous unknown or assumed conditions, such as ground anisotropy, stress conditions, and variable geotechnical parameters, it is difficult to accurately predict surface deformation by conventional methods (Galera et al., 2007). To address this issue, preliminary monitoring of each location is essential. As shown in Fig. 1, the pre-shield arrival surface settlement (S_{PS}) was used as a time input parameter, and S_S was mapped together with other influencing parameters.

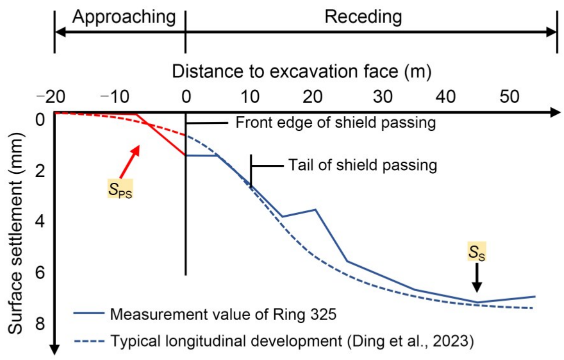

Fig. 1 Schematic of typical longitudinal development (Ding et al., 2013) and parameter selection of surface settlement

2.2 Strategy of adaptive adjustment

The EPB shield (model ZTE6250) has a reliable synchronized grouting, propulsion, measurement, and grading system, which adjusts the grouting pressure and speed according to the real-time shield tail gap data and changes the advance speed and attitude by controlling the jacking thrust. In practical engineering applications, it is necessary to take into account the controllable nature and interactive synergies of parameters with the advance speed, cutter head rotating speed, and screw conveyor rotating speed (S_A, R_C, and R_{SC}), being directly determined by the operator, but with the total thrust (T_T), support pressure (P_S), and cutterhead torque (T_C), and other parameters being jointly influenced by controllable parameters as well as geometric and ground conditions (Li et al., 2021; Wang et al., 2024). In addition, there are varying interaction effects between these parameters, as shown in Fig. S2 of the ESM, which is similar to the topology network structure.

While searching all parameters can yield the optimal outcome, doing so might disrupt the inherent interactive relationships between the parameters. To address this, by leveraging the distinctive advantages of ML methods in dealing with problems of high coupling among influencing factors and indeterminate reasoning rules, this paper introduces an innovative method that employs a combination of optimization and inverse prediction strategies, minimizing the impact of the interaction between shield parameters. This methodology is designed to realize the self-adaptation of shield machinery, with its summary illustrated in

Fig. 2. The entire procedure is bifurcated into design phase I and construction phase II.

Phase I begins with the development of a prediction model of S_s (Model 1), which is then utilized as a meta-model for conducting parameter sensitivity analyses and other operations. A multiclassification method for shield operation parameters is developed to target the control of settlement. Operation parameters with high global sensitivity are classified as Category A parameters, and those with low global sensitivity are classified as Category B (uncontrollable) and Category C (controllable) parameters according to whether they are artificially regulated. The first step in the adaptive adjustment mechanism involves recommendations for Category A parameters, which determine the settlement through an integration of the settlement prediction model with the PSO algorithm. In contrast, parameters of Categories B and C, which possess low global sensitivity, are initialized with their respective mean values as model inputs. In the second step, as illustrated in Fig. 3 (which presents a detailed view of the inversion prediction module in Step 2 of Fig. 2), the updated Category A parameters, in tandem with geometric and geotechnical parameters as well as settlements, are used to inversely derive new Category B parameters through Model 2. This is followed by the inverse prediction of Category C parameters and all the aforementioned parameters through Model 3, which makes it possible to recommend human-controllable parameters more precisely by adding input parameter dimensions. At this point, the entire optimization workflow is complete. This strategy optimizes resources by focusing on parameters that play a dominant role in settlement, significantly reducing computational complexity. At the same time, it maximizes the retention of parameter interactions, avoids the optimization bias caused by traditional methods that ignore parameter correlations, and more accurately reflects the impact of parameter synergies on tunneling-induced settlement.

Phase II is dedicated to developing the SPOS, as shown in Fig. S3 of the ESM, for comprehensive settlement control in shield tunneling. The optimized parameters are transmitted to the shield machine operator for real-time tuning. During the construction of the shield tunnel, new monitoring data samples are constantly being generated. These will be helpful in future research for further improving the accuracy of the prediction model and enhancing the accuracy of the recommended parameters of the system.

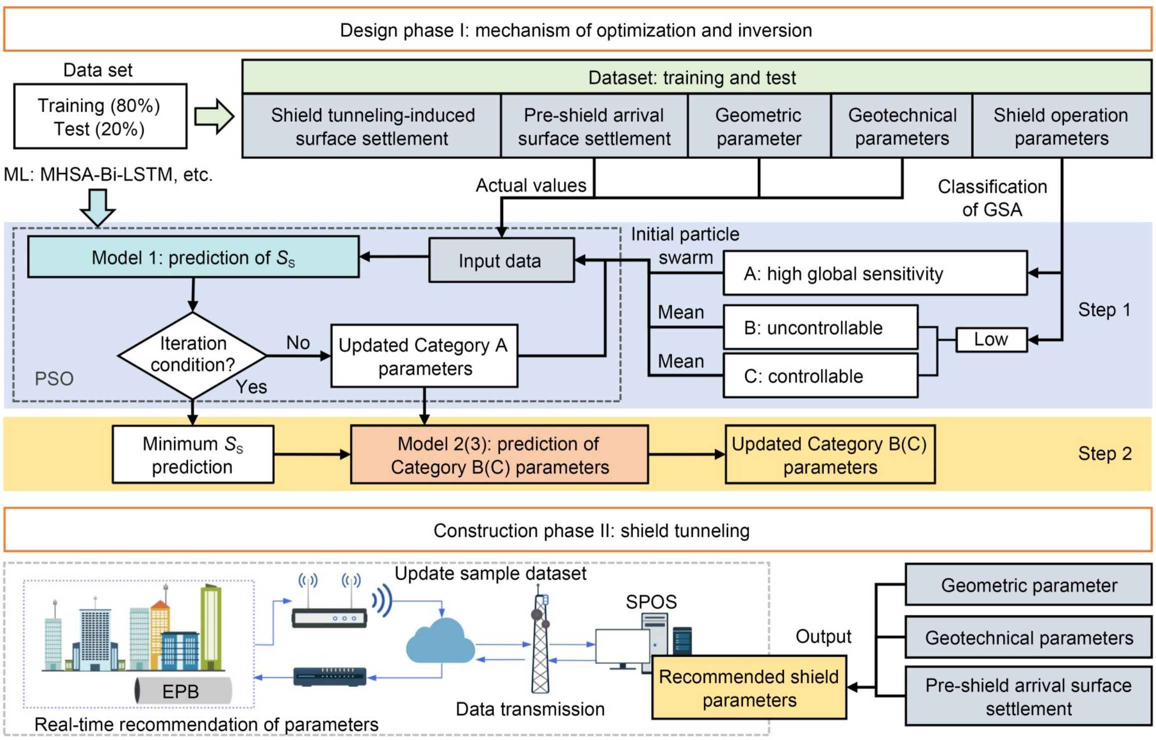

Fig. 2 Schematic diagram of the self-adaptation method of EPB shield tunneling. GSA is the global sensitivity analysis; PSO is the particle swarm optimization; SPOS is the shield parameter optimization system

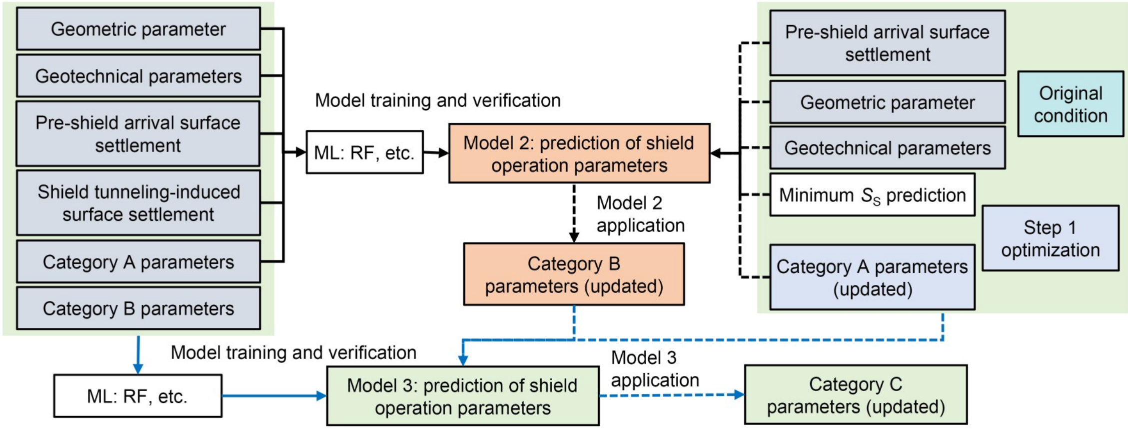

Fig. 3 Inversion prediction of shield operation parameters of Categories B and C

In addition, the principle of Bi-LSTM is presented in Section S1 and Fig. S4 of the ESM; the principle of MHSA is presented in Section S2 and Fig. S5 of the ESM; the principles of RF and PSO are presented in Sections S3 and S4 of the ESM, respectively; the performance indicators are presented in Section S5 of the ESM.

3 Case study

3.1 Project overview

This section presents an analysis using the Changchun twin-tunnel metro construction project as a case study and validates the proposed model. The specific section analyzed is the shield tunneling interval between Feiyue Square Station and Eurasia Shopping Mall Station on the 2nd section of Line 6 of the Changchun Metro (ZK16+197.489 to ZK17+575.235), with the shield excavation proceeding from Eurasia Shopping Mall Station toward Feiyue Square Station in the northwest direction, as depicted in Fig. 4a. Spanning a length of 1372.44 m, the interval features a minimum curve radius of 550.00 m and a maximum line gradient of 1.3268%. The overburden above the shield tunnel ranges from 8.70 to 12.30 m. The tunnel excavation occurred in the northwest direction, crossing underneath rain and sewage pipes as well as gas pipelines and running parallel to the Feiyue Road Tunnel. Two EPB shields of model ZTE 6250 from China Railway Construction Heavy Industry Co., Ltd. were used, each with a cutterhead diameter of 6.28 m. As shown in Fig. S6 of the ESM, the cutterhead of the shield is a composite type (four-spoke+panel configuration) with an opening ratio of approximately 38%. The cutterhead is equipped with four double-edge toothed cutters at the center, 21 front single-edge toothed cutters, 30 scrapers, 11 edge single-edge alloy disc cutters, and eight pairs of edge scrapers for bore diameter calibration. The tunnel lining consists of segments with an outer diameter of 6.20 m, a thickness of 0.35 m, and a length of 1.50 m. The center-to-center distance between the twin tunnel axes ranges from 13 to 17 m.

Fig. 4b illustrates the comprehensive geological cross-section of the shield tunneling interval for the northwest travel direction line. The topography of this interval is predominantly flat with an overall gradient from west to east. The stratigraphic description from the uppermost to the lowermost layer is as follows: miscellaneous fill layer (1) primarily is consists of cohesive soil and construction waste, characterized by a loose structure and inconsistent density, with some areas featuring man-made pavement layers; silty clay fill layer $(2)_1$ is plastic in consistency, mainly composed of arable soil with root systems and a minor content of crushed stones; silty clay layer $(2)_2$ is plastic and slightly soft; completely weathered mudstone layer $(3)_1$, intensely weathered mudstone layer $(3)_2$, and moderately weathered mudstone layer $(3)_3$ are susceptible to disintegration upon long-term exposure and readily soften when wet. Table 1 shows the physical and mechanical properties of the geotechnical materials in each layer below the Feiyue Road Tunnel. The groundwater table is at a depth of 1.20 to 9.20 m, with an altitude between 195.15 and 229.21 m, predominantly sustained by lateral seepage and throughflow replenishment.

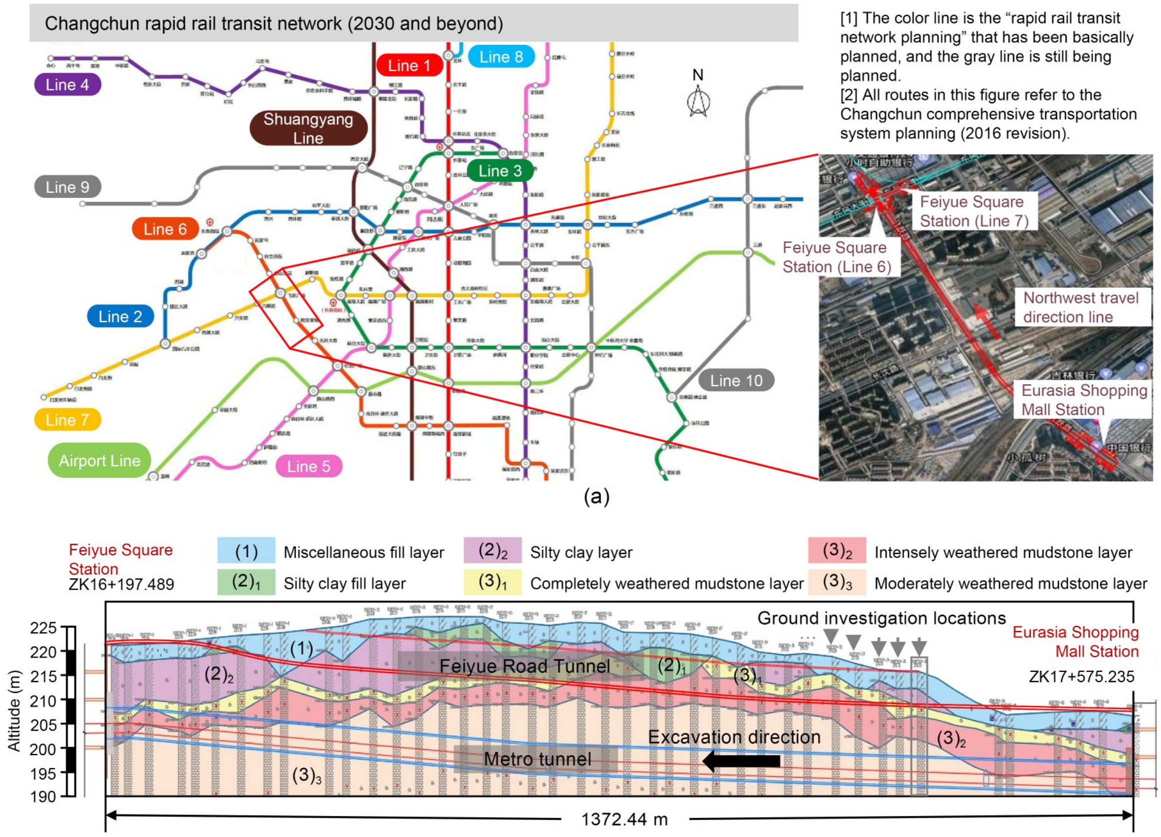

Fig. 4 Location of construction site: (a) plan view; (b) geological profile

Table 1 Statistics of the physical and mechanical properties of geotechnical materials

Geotechnical material	Density, ρ (kg/m^3)	Depth (m)	Water content (%)	Void ratio, e	Liquid limit, W_L (%)	Plastic limit, W_P (%)	Constrained modulus, E_{oed} (MPa)	Cohesion, c (kPa)	Angle of internal friction, φ (°)	Lateral earth pressure coefficient at rest, K_0
Miscellaneous fill layer (1)	1900	0.2–5.5	22.0	0.84	34.5	19.5	5.5	25	18	0.440
Silty clay fill layer (2)$_1$	–	0.2–9.1	–	–	–	–	–	–	–	–
Silty clay layer (2)$_2$	1960	0.4–16.0	19.9	0.79	28.5	16.5	5.9	29	20	0.425
Completely weathered mudstone layer (3)$_1$	2030	1.5–13.7	18.3	0.72	28.8	18.1	6.2	27	22	0.390
Intensely weathered mudstone layer (3)$_2$	2020	2.0–31.0	17.3	0.68	28.3	17.7	7.4	43	23	0.360
Moderately weathered mudstone layer (3)$_3$	2020	5.4–48.0	15.7	0.62	27.5	17.0	9.9	52	25	0.330

E_{oed} is determined from oedometer tests over the stress increment range of 100 to 200 kPa (GB/T 50123-2019 (MOHURD and SAMR, 2019)). K_0 is determined from laboratory K_0 consolidation tests. The values are lower than those predicted by Jaky's formula for normally consolidated soils, reflecting the residual structural stiffness of the weathered rock mass

3.2 Data preprocessing

3.2.1 Data source

A total of 100 sets of parameter values, a sample size comparable to recent shield tunneling ML studies (31–137 samples) (Ye et al., 2023; Zhou Z et al., 2023; Dong et al., 2025; Li et al., 2025), were sampled from Ring 170 (at ZK17+321.735 on 2022/1/3) to Ring 665 (at ZK16+579.235 on 2022/5/01), with a interval of five rings, situated below the Feiyue Road Tunnel. The overall structural integrity of the tunnel in this interval reduces the deformation induced by shield tunneling, and the impact of adjacent rings is more significant and cannot be disregarded. Consequently, this presents challenges for conventional ML modeling approaches.

3.2.2 Fusion of multisource heterogeneous data

Within the framework of Model 1, the influence of a total of 17 variables on the ultimate settlement was examined. The shield tunneling and settlement data are represented in the spatiotemporal domain, where each set of data corresponds to a specific time and location. The geometric and geotechnical parameters are represented in the spatial domain, where each parameter record corresponds to a specific location along the tunneling trajectory. The data fusion process is depicted in Fig. S7 of the ESM.

Geometric and geotechnical parameters were determined from the ground investigation report (GIR). It should be pointed out that the geotechnical parameters given in Table 1 are in the form of mean values. The actual ground investigation locations are shown in Fig. 4b, where separate tests were conducted at each corresponding location to obtain the parameter values. The root cause of surface settlement during shield tunneling is attributed to the disturbance of the surrounding soil matrix due to construction activities, resulting in a redistribution of soil position and stress. Specifically, the overburden soil above the shield tunnel, being in the direct impact zone of the construction, experienced the most pronounced effects. Therefore, the test results of different soil layers at each sampling position were interpolated linearly and mapped onto each shield ring position. The physical and mechanical parameters were weighted according to the thickness of different soil layers and averaged, as shown in Fig. S7 of the ESM.

The shield operation parameters were monitored by the system in real time, removing data from the shutdown phase using parametric multiplication methods (Zhang et al., 2022; Chen et al., 2023). Given the noncontinuous nature of the construction process, specific data selection was refined to minimize the effects of noise and outliers. The excavation chamber behind the cutterhead is typically maintained at a level between half-full and full, and P_S was determined by averaging the pressure at the excavation face. Parameters such as S_A and R_C were determined by the average of the corresponding ring positions.

To synchronize the surface settlement data with shield operation parameters, measurements were taken along the longitudinal axis of the tunnel at the same intervals of 7.5 m for 12 h, with an increased monitoring frequency of 3 h near the shield excavation position. The maximum surface settlement recorded within 10 d after the completion of ring boring was used as S_S. The pre-shield arrival surface settlements $S_{PS,0}$ and $S_{PS,7.5}$ are the surface settlements at a location when the shield arrives at that location and when the shield is 7.5 m before arriving at that location.

3.2.3 Data division and standardization

The first 80% of the datasets were used for the training dataset, and the remaining 20% of the data constituted the test dataset, which was used to validate the accuracy and validity of the predictive model. Table S1 of the ESM delineates the input and output parameters within Model 1 along with their respective value ranges.

The parameters of the samples encompassed disparate units of measurement and exhibited substantially different value ranges. Direct model training without prior adjustment could result in a degradation of accuracy. To bolster the precision of the model's predictions and to hasten the convergence of algorithms, the training data underwent min–max normalization, transforming it to the interval of [0, 1].

4 Results and discussion

4.1 Settlement prediction and comparative analysis

In the conceptualization of Model 1, as a successor to traditional empirical or numerical models, prediction accuracy was prioritized. While increasing hidden layers can capture complex patterns, 1–3 layers balance complexity and performance (Shen et al., 2021). As shown in Fig. S8 of the ESM, a two-layer Bi-LSTM architecture was adopted. The first Bi-LSTM layer (L1) processed sequential features bidirectionally, capturing short-term dependencies. An SA layer followed L1, projecting its output into h subspaces (heads) to compute contextual weights. A dropout layer regularized the attention output to prevent overfitting. The second Bi-LSTM layer (L2) integrated attention-weighted features, enhancing long-term dependency capture through bidirectional recurrence. The optimizer was configured to adaptive moment estimation, with the training process set to complete after 500 epochs. To mitigate instability during the training process, the learning rate was modulated using a piecewise schedule strategy, commencing with an initial learning rate (r_l) of 0.001 (dimensionless), with the learning rate reduced by a drop factor of 0.15 after 400 epochs. The grid search method (GSM) was used to determine various hyperparameters in the model, including the stride sequence [1:1:5] (searched over 1 to 5 in a increment of 1, the following text is similar), the number of hidden units (n_{hs1} and n_{hs2}) [10:10:500] in the Bi-LSTM layer, the dropout rate (r_{dp}) [0.10:0.05:0.60] in the dropout layer, the number of heads [2:1:10], and the number of key channels [1:1:10 times the number of heads] in the SA layer. The five-fold time-series cross-validation (5-TCV) method was utilized to determine the optimal architecture of the proposed models. The comparative analysis involved four extensively utilized models: SVR (Sun, 2022), RF (Zhang et al., 2020c), Transformer, and Bi-LSTM (Zhou Z et al., 2023). For these comparative models, the quantities of input and output parameter units, as well as the number of training epochs, were consistent with those of the MHSA-Bi-LSTM model. The remaining hyperparameters were optimally determined using the GSM. The aforementioned modeling procedures were executed in MATLAB software and Python (version 3.10), and the specific hyperparameter settings determined for the models are detailed in Table 2.

The models were trained based on their respective structural parameters, and the test set was employed to conduct predictive analyses for each model. The predicted results and relative errors are depicted in Fig. 5. All samples were predicted, and the predicted results and evaluation indicators of each model were obtained, as shown in Fig. S9 of the ESM.

Table 2 Optimum hyperparameters in ML models

Model	Hyperparameter	Value
MHSA-Bi-LSTM	Stride sequence	2
	Number of key channels	20
	Number of heads	4
	n_{hs1}	120
	n_{hs2}	80
	r_{dp}	0.5
	r_l	0.001
	Batch size	20
Bi-LSTM	Stride sequence	2
	n_{hs1}	200
	n_{hs2}	160
	r_{dp}	0.3
	r_l	0.001
	Batch size	20
Transformer	Stride sequence	1
	Embed dim	31
	Number of heads	1
	Feedforward network dim	16
	r_{dp}	0.28
	r_l	0.001
RF*	Number of decision trees, n_{tr}	136
	Minimum number of leaf node samples, n_{lf}	5
SVR*	Penalty parameter, C	1.414
	Smoothing parameter of kernel function, g	0.707

Models marked with '*' are unable to capture the spatial features of S_S due to structural limitations

Fig. 5 illustrates that over 90% of the relative errors for the test set predictions from the five models are contained within 20%. This signifies the capability of ML techniques to discern the intrinsic correlations between shield operation parameters, geotechnical parameters, and shield settlement, indicating that the selection of input parameters is reasonably justified.

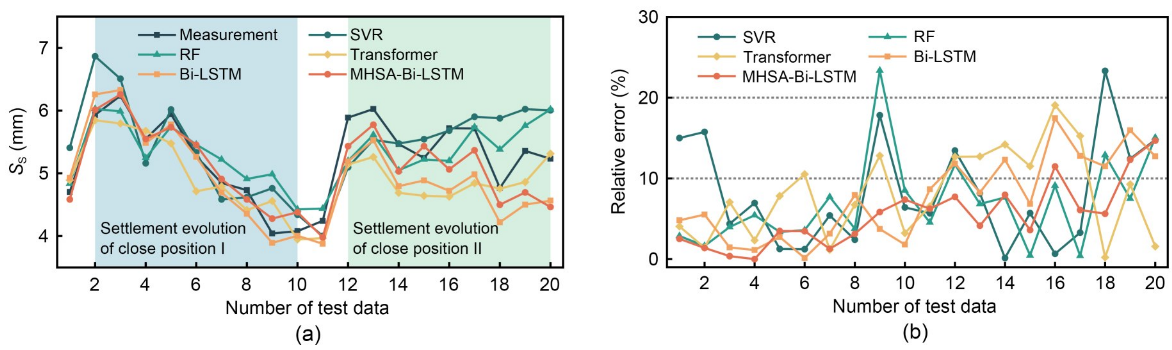

Fig. 5 (a) Predicted results and (b) relative errors of the test set

Additionally, the input of S_{PS} gives the model a good predictive performance. In contrast to the average relative errors of 8.21% for the SVR model, 7.02% for the RF model, 8.00% for the Transformer model, and 7.54% for the Bi-LSTM model, the MHSA-Bi-LSTM model has achieved a reduction to 5.22%, with the prediction errors for 85% of the samples being confined within 10%. However, in the other models, the samples satisfying this criterion have not surpassed 80%. As depicted in Fig. 5a, the Transformer, Bi-LSTM, and MHSA-Bi-LSTM models have almost perfectly captured the spatial correlation across two distinct intervals. The latter effectively focused on important features, resulting in predicted results closer to the actual measurements. Overall, the MHSA-Bi-LSTM model exhibited superior performance in predictive accuracy and error stability.

Fig. S9 of the ESM shows the predictive performance of each model. The closer the scatter points are to the diagonal, the more accurate the model's predictions. The SVR model, which constructs a hyperplane or an approximation function in high-dimensional feature space for regression, tends to determine a cautious predicted value to samples to account for uncertainties, and thus trading off some level of precision. The RF model is not able to capture spatial relationships due to structural limitations and showed good performance with the training set but not the best performance with the test set. Although both the Transformer and Bi-LSTM models have the ability to capture long-term dependencies, the former performs unsatisfactorily on the training and validation sets, while the latter has a better overall performance. The MHSA-Bi-LSTM model outperformed all the other models in the test set for S_S prediction, with mean absolute error (MAE), root mean square error (RMSE), and coefficient of determination (R^2) values of 0.283, 0.352, and 0.780, respectively. This superior performance is credited to its enhanced memory retention and attention mechanisms, indicating that the model possesses optimal predictive accuracy for forecasting the surface settlement during shield tunneling operations.

Fig. 6 shows the standard Taylor diagram (Taylor, 2001) of the predicted results of all the models, where the black dashed lines represent the Pearson correlation coefficient (r), the blue dotted lines represent the root mean squared difference (RMSD, which is conceptually related but not identical to RMSE), the solid lines represent the standard deviation, and the red dot

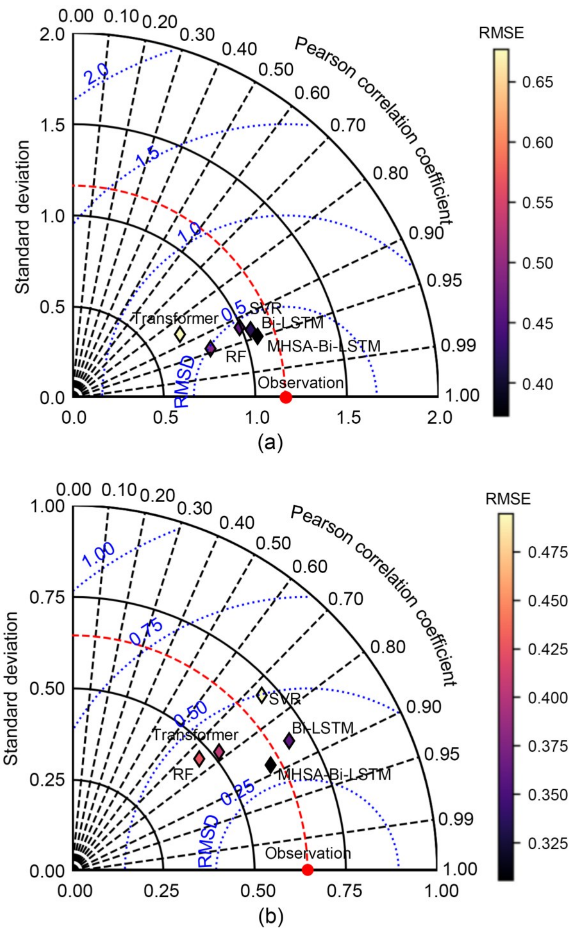

Fig. 6 Standard Taylor diagrams of the predicted results of all the models: (a) training and validation sets; (b) test set

represents the observation point. The closer each index value is to the observation point, the more accurate the prediction results are. It is obvious that the MHSA-Bi-LSTM model is closer to the observation point compared to other models, which means it is more competitive than the other models.

4.2 Sensitivity analysis of parameters affecting S_S

Sensitivity analysis methodologies are instrumental in determining the importance of input variables to models or systems and are frequently applied to evaluate the degree of output variation attributable to parameter uncertainties, significantly contributing to the identification of parameter priorities and dimension reduction (Liu and Ding, 2020). Despite the computational simplicity and speed of local sensitivity analysis (LSA), its heavy reliance on nominal value positions and lack of insight into the true value locations make it inappropriate for shield tunneling systems characterized by high levels of parameter uncertainty (Cheng et al., 2016). GSA, on the other hand, captures the influence of the entire input parameter space on the model outcomes, independent of the need to predefine optimal positions and effectively circumvent the constraints of LSA.

This research employs the Sobol' method (Sobol', 2001; Liu and Ding, 2020) within GSA to examine the extent to which various parameters affect S_S. Suppose the proxy model is $Y=f(\boldsymbol{X})$ and $\boldsymbol{X}=(X_1, X_2, \cdots, X_t)^T$, where $\boldsymbol{X}$ is the input variable vector, X_i (i=1, 2, $\cdots$, t) is the ith input variable, and t is the number of input variables. The unconditional variance $V(Y)$ can be decomposed into partial variances accordingly, where V_i (i=1, 2, $\cdots$, t) and $V_{i,j}$ (i=1, 2, $\cdots$, $t-1$; $j=i+1$, $i+2$, $\cdots$, t) represent the variances of main-effect function components f_i and interaction-effect function components $f_{i,j}$, respectively.

$$V(Y)=\int_\Omega f^2(\boldsymbol{X})\mathrm{d}\boldsymbol{X}-f_0^2=\sum_{i=1}^{t}V_i+\sum_{i=1}^{t-1}\sum_{j=i+1}^{t}V_{i,j}+\cdots+V_{1,2,\cdots,t}, \tag{1}$$

where Ω is the integration domain defined over the unit hypercube; f_0 is the constant mean value of the function $f(\boldsymbol{X})$; $V_{1,2,\cdots,t}$ is the partial variance attributable to the high-order interaction of all t input parameters.

Using these variations, first-order, second-order, and total Sobol' sensitivity indicators can be defined according to the total variance:

$$S_i=\frac{V_i}{V(Y)}=\frac{V_{x_i}\left[E_{\boldsymbol{X}\sim x_i}(Y|x_i)\right]}{V(Y)}, \tag{2}$$

$$S_{i,j}=\frac{V_{i,j}}{V(Y)}=\frac{V_{x_i,x_j}\left[E_{\boldsymbol{X}\sim x_i,x_j}\left(Y|\boldsymbol{X}\sim x_i,\ x_j\right)\right]}{V(Y)}, \tag{3}$$

$$S_i^T=1-\frac{V_{\sim i}}{V(Y)}=\frac{E_{\boldsymbol{X}\sim x_i,x_j}\left[V_{x_i,x_j}(Y|\boldsymbol{X}\sim x_i)\right]}{V(Y)}, \tag{4}$$

where S_i is the main sensitivity index (MSI), indicating the degree of disturbance to the output when a single input x_i fluctuates; V_{x_i} is the variance operator with respect to the input variable x_i; $E_{\boldsymbol{X}\sim x_i}$ is the expectation operator with respect to all input variables except x_i; $S_{i,j}$ is the second-order interaction effect index, indicating the degree of disturbance to the output caused by the interaction between the two inputs x_i and x_j; V_{x_i,x_j} is the variance operator with respect to the input variables x_i and x_j; $E_{\boldsymbol{X}\sim x_i,x_j}$ is the expectation operator with respect to all input variables except x_i and x_j; $V_{\sim i}$ is the bias variance corresponding to the remaining indicators except x_i; S_i^T is the total sensitivity index (TSI), indicating the total degree of disturbance of the output by all the effects caused by the fluctuation of input indicator x_i and can be interpreted as the sum of the sensitivity indices of each order for that input indicator.

Utilizing the MHSA-Bi-LSTM model constructed as a surrogate model and based on the parameter variable range, Latin hypercube sampling (LHS) (Dige and Diwekar, 2018) is performed, followed by correlation computations to determine the MSI and TSI for each parameter across different sample magnitudes, as illustrated in Fig. 7.

Overall, when the sampling magnitude exceeds 2^{11}, the ranking of sensitive input parameters by MSI and TSI is stable. The primary and total effects of the parameters exhibit no marked variations in their order, suggesting that the interactive effects among inputs have a limited impact on the surface settlement. As evident from the stable sensitivity index values in Figs. 7b and 7d, the effects of $S_{PS,0}$, $S_{PS,7.5}$, and uncontrollable geometric and geotechnical conditions have a certain degree of influence on S_S, with their aggregate TSI values summing to approximately 0.5. In the calculation results, the MSI and TSI of V_E, P_S, R_C, and T_C are relatively large, indicating that these parameters have a great influence on S_S. Consequently, these parameter indicators should be prioritized during the optimization and control processes for S_S.

4.3 Operation parameter adjustment based on the integration mechanism

The workflow mechanism in Fig. 3 indicates that the selection of Category A parameters is pivotal in determining the extent of optimization, whereas parameters of Categories B and C delineate the interdependencies among the operation parameters. To balance optimization effectiveness with practical application scenarios, this study assessed the S_S optimization capabilities with varying numbers of Category A parameters. At most, the top five most sensitive parameters were selected for optimal search as Category A parameters, since at this point (Fig. 8a), the cumulative

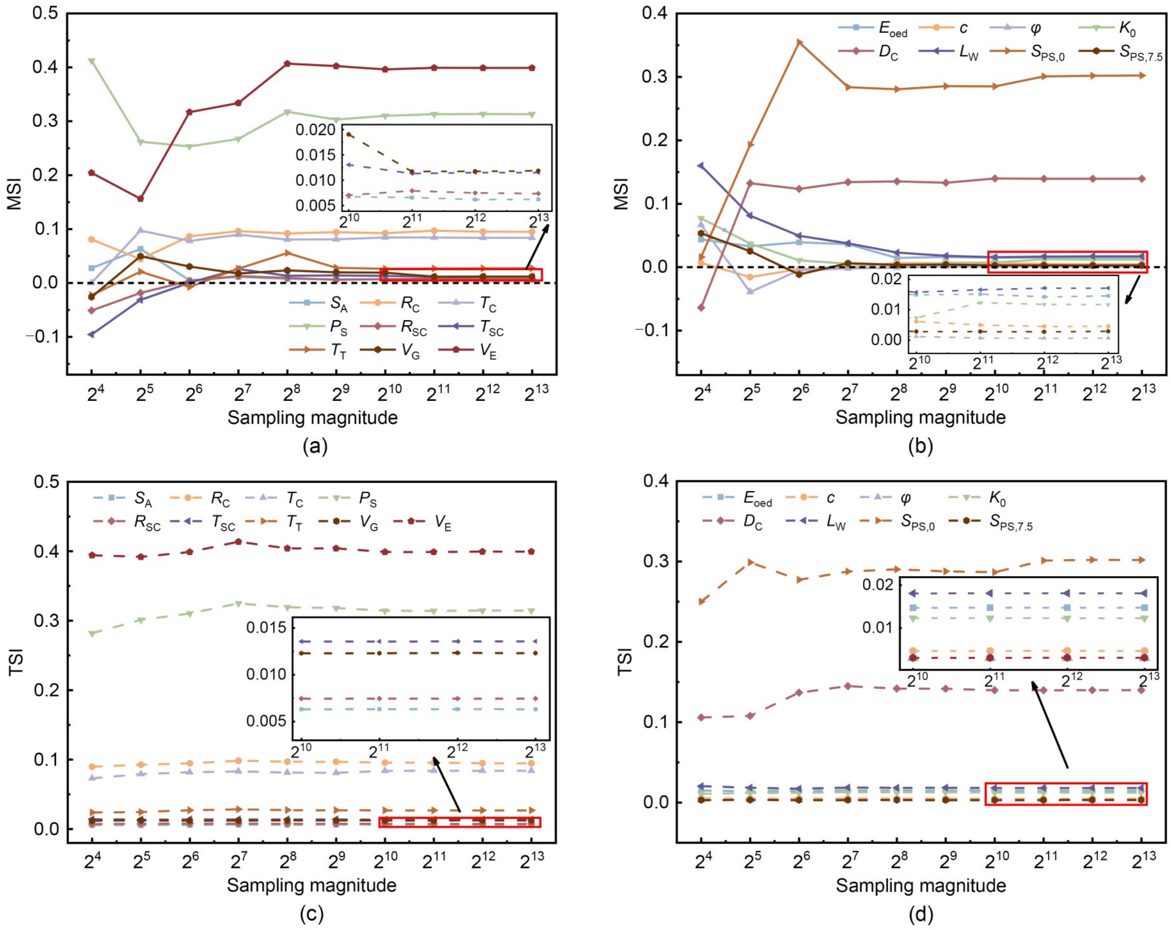

Fig. 7 Parameter sensitivity: (a) MSI of shield operation parameters; (b) MSI of geometric and geotechnical parameters; (c) TSI of shield operation parameters; (d) TSI of geometric and geotechnical parameters

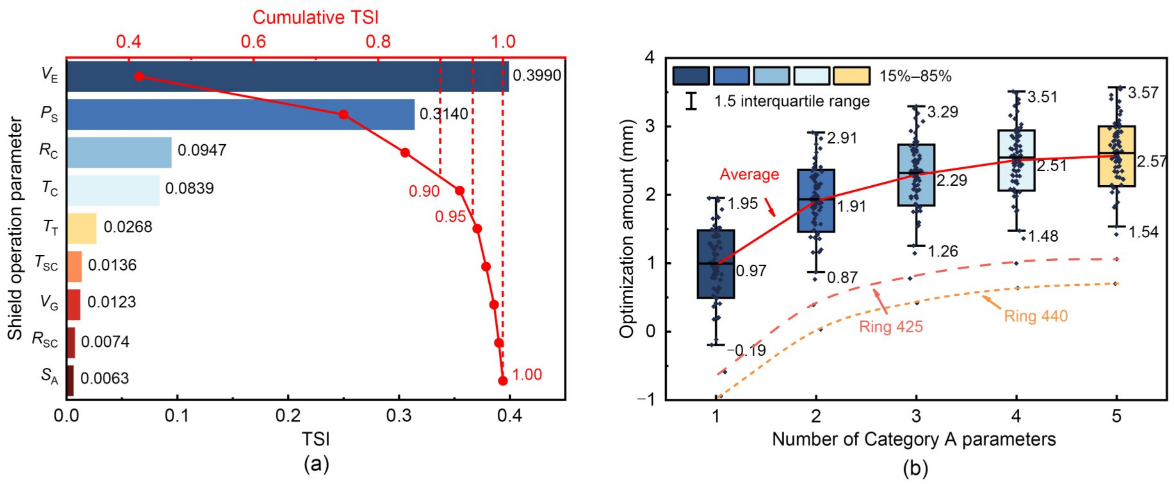

Fig. 8 (a) TSI results of shield operation parameters and cumulative TSI; (b) optimization amount of S_S for the training set under different numbers of Category A parameters

TSI results are over 0.90 and have absolute influence. The PSO method was employed as an optimization approach for Category A parameters. The S_S outcomes forecasted by the meta-model were adopted as the fitness function for PSO. The position vector within the PSO method was substituted with the Category

A parameters that were targeted for optimization. The goal of the algorithm was to determine a suitable position vector, that is, the shield operation parameters, which resulted in the minimization of the fitness value. Within the PSO method, the iteration count was fixed at 100, the swarm size was 50, the acceleration coefficients (C_1 and C_2) were 1.5, and the inertia weight (w) was 0.8. The range of parameter values was determined by the extremities of the monitored data. The detailed procedures are outlined in Section S4 of the ESM, and the S_S optimization amount (the difference between the predicted output values of the unoptimized model and the optimized model) derived from the training set is depicted in Fig. 8b.

Fig. 8b shows that most of the optimized results are markedly lower than the unoptimized model predictions, with minimal optimization effects observed for Ring 425 and Ring 440. This suggests that the geometric and geotechnical parameters are predominantly responsible for S_S at these points, while the influence of the shield operation parameters is comparatively minor. However, the optimization plateaus when the number of Category A parameters exceeds four. Due to the waning global sensitivity of the additional parameters and the persistent impact of geometric and geotechnical parameters in the meta-model, the optimization speed of the predicted S_S value slows down and gradually converges.

In the four-parameter optimization, the optimized recommended values of V_E, P_S, R_C, and T_C for each ring position are located at extreme values of 63.09 m^3 (min), 1.5 bar (max), 1.5 r/min (min), and 1.4 MN·m (min), respectively. This is not difficult to explain and indicates that within the constrained range, there is a strong monotonic relationship between these input parameters and S_S. Specifically, a decrease in V_E, R_C, and T_C results in diminished disturbance to the excavation face and the soil surrounding the shield, consequently yielding relatively reduced surface settlement. Conversely, an altitude in P_S creates a more densely compacted zone ahead of the shield, where soil particles undergo compaction, enhancing the soil density and reducing its compressibility. This reduction in compressibility subsequently mitigates ground surface settlement. These observations further substantiate the alignment of the mapping relationship with reality.

As shown in Fig. 9, there are varying degrees of correlation among the shield operation parameters, where a r greater than 0.200 indicates a certain degree

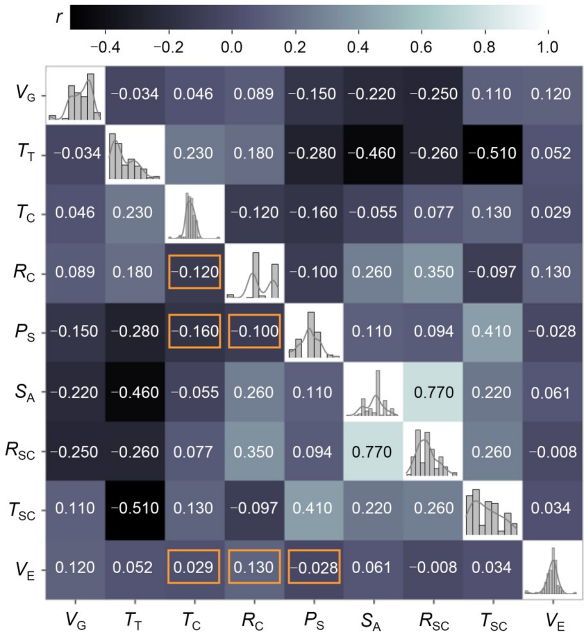

Fig. 9 Correlation matrix heatmap of shield operation parameters

of correlation. Optimizing all the parameters completely destroys this intrinsic relationship, leading to physically unrealistic combinations. The cells highlighted with orange borders denote the six pairwise r values among the four Category A parameters (V_E, P_S, R_C, and T_C). All highlighted values exhibit low absolute r values ($|r|\leqslant 0.2$), confirming that these four parameters are largely mutually independent. This weak intercorrelation supports the selection of four Category A parameters for direct optimization, as adjusting them simultaneously does not severely disrupt the intrinsic relationships within the operation parameter system.

On the main diagonal of Fig. 9, frequency distribution histograms are presented for each individual parameter in place of the trivial self-correlation value of 1.000. For instance, the detailed fitted distributions of T_C and V_E are presented in Fig. S12 of the ESM, where their implications for the interpretation of optimization results are discussed.

Many interactions between parameters have been discovered, such as V_E being intricately linked to stratum parameters (S_A, R_{SC}, and T_{SC}) (Huang et al., 2022). Similarly, P_S is closely associated with T_T, S_A, T_C, R_C, R_{SC}, T_{SC}, etc. (Lin et al., 2021). To attain more accurate recommendations while conforming to practical conditions on site, a hierarchical inversion method is introduced. As shown in Fig. 3, the study primarily employs inverse Model 2 to backtrack uncontrollable Category B parameters (T_T, T_{SC}, and V_G), using geometric and geotechnical parameters, updated Category A parameters, and settlements as inputs. Subsequently, artificially regulated parameters of Category C (R_{SC} and S_A) are backtracked in Model 3 using all the aforementioned parameters (updated). The variable details for Models 2 and 3 are presented in Table S2 of the ESM.

In the data distribution, it was found that some of the operation parameters that need to be inverted have limited monitoring accuracy. Models such as LSTM and Transformer are based on back-propagation algorithms, which may affect the state update in subsequent sequence steps and can lead to large deviations in the predicted results (Rashid et al., 2018; Tsai and Cho, 2021). Ensemble learning algorithms, such as RF, exhibit good stability and robustness when data anomalies occur (Hia et al., 2023) and are used for inversion prediction of parameters of Categories B and C. The SVR model, which also exhibits excellent robustness (Hou et al., 2020), is used for comparison. GSM and 5-TCV are used as hyperparameter optimization methods.

Figs. S10 and S11 of the ESM show the predicted and inversion results for shield operation parameters using Models 2 and 3, respectively. The prediction performance of the five parameters is generally good. The distribution of some Category B parameters is more concentrated due to the limitation of monitoring accuracy, which will inevitably be affected in the inversion prediction. The adjustment steps set by the staff for the Category C parameters are large, and the positions of many points are fixed, which leads to some deviations in the predicted results. The SVR model is more susceptible to monitoring accuracy, resulting in increased errors, while the RF model has superior predictive performance, with average reductions of 27.46% and 27.03% in MAE and RMSE in the test set, respectively. It is obvious that the MAE and RMSE values of the T_{SC} and S_A are much higher than those of the remaining three parameters because the order of magnitude and the range of T_{SC} and S_A are larger than those of the other shield operation parameters.

In practical engineering applications, the primary concern is reasonable control, followed by avoiding frequent adjustments, which indicates that the inversion of operating parameters requires higher precision. Fig. S10 of the ESM shows that the range of variation in the controllable parameter inversion results of the SVR model is very small, which is abnormal in practice. For example, take the R_{SC}–S_A (Fig. 9), which exhibits the most significant linear relationship (r=0.770), as an example and perform a Fisher's Z test. As shown in Fig. 10, when using the RF and SVR models, the Z values for the correlation coefficients between the inversion results and the initial values are −1.427 and 1.029 (<1.96), with p values of 0.153 and 0.303 (>0.05), respectively, indicating that the differences in correlation coefficients are not significant. The slope difference of the RF model is 0.667, the t-statistic is 1.723 (<1.96), and the p value is 0.087 (>0.05), indicating no significant difference in the linear relationship between the data before and after inversion. However, the slope difference of the SVR model is −2.677, the t-statistic is −9.120 (<−1.96), and the p value is extremely small (2.22×10^{-16}), indicating a highly significant difference. In contrast, the

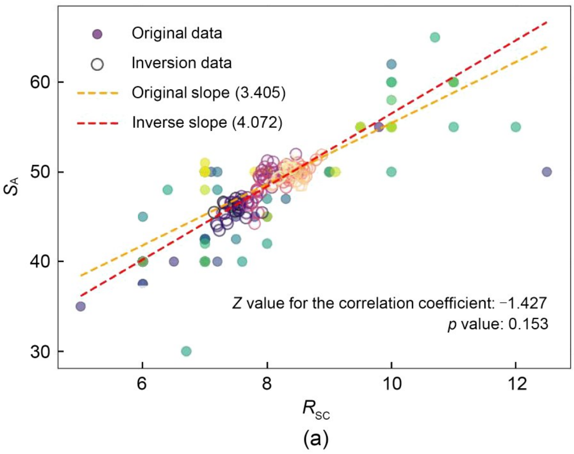

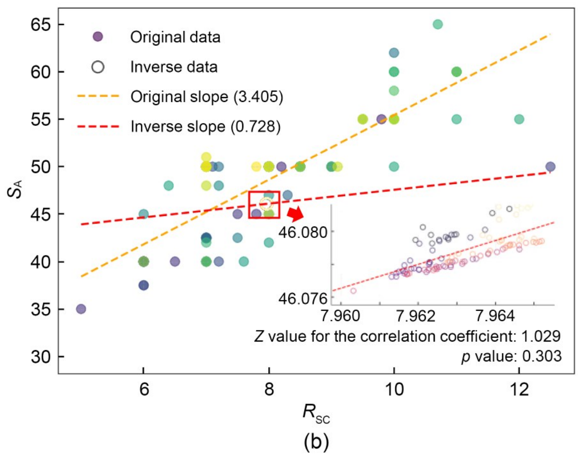

Fig. 10 Scattered distribution of R_{SC}–S_A: (a) RF; (b) SVR

RF model performs exceptionally well, which is more appropriate for consideration.

4.4 Mechanism verification and qualification

To evaluate the reliability and feasibility of the research framework for shield parameter self-adaptation, the updated parameters, following the completion of all optimization procedures, are introduced in place of the initial operation parameters into the settlement prediction meta-model. Given that the precision of Model 1 has been confirmed in prior sections, it is justifiable to regard the new predictive outcomes as reliable. By adjusting the parameters of the test set using the proposed method, the optimized S_S obtained are shown in Fig. 11.

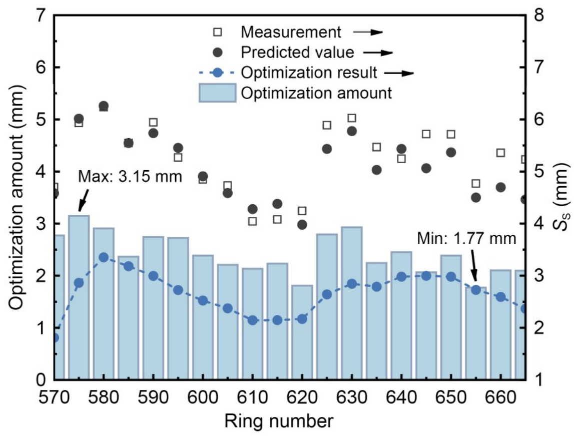

Fig. 11 Results of the adaptive adjustment strategy in the test set

The results in Fig. 11 show that the optimized S_S was reduced for all ring positions in the test set. The predicted S_S of the adaptive adjustment strategy was reduced by an average of 2.41 mm (47.55%). A comparison with the actual measurements shows that, with a few exceptions, the S_S was significantly reduced by an average of 2.59 mm (49.28%). In conclusion, the integration mechanism of optimization and inversion shows a strong ability to control settlement.

In subsequent shield construction, the adaptive adjustment strategy proposed in this study (applied to Rings 815–910) contrasts sharply with the full optimization strategy proposed by Hou et al. (2020) (applied to Rings 715–810), mainly using the minimum S_S as the objective function and directly searching all shield operation parameters through an optimization algorithm. As shown in Fig. 12, the full optimization strategy performs global optimization of all the operation parameters without distinguishing between the controllability and sensitivity differences of parameters, leading to adjustments of uncontrollable parameters (such as T_T, V_G, and T_{SC}) deviating from actual engineering constraints. In contrast, the adaptive mechanism considers the synergistic values of all the shield operation parameters under all geometric and ground conditions, with adjustments to uncontrollable parameters better aligning with actual engineering constraints. Notably, there is a certain discrepancy between the recommended results (minimum values) for T_C and V_E and the actual results. This is because the

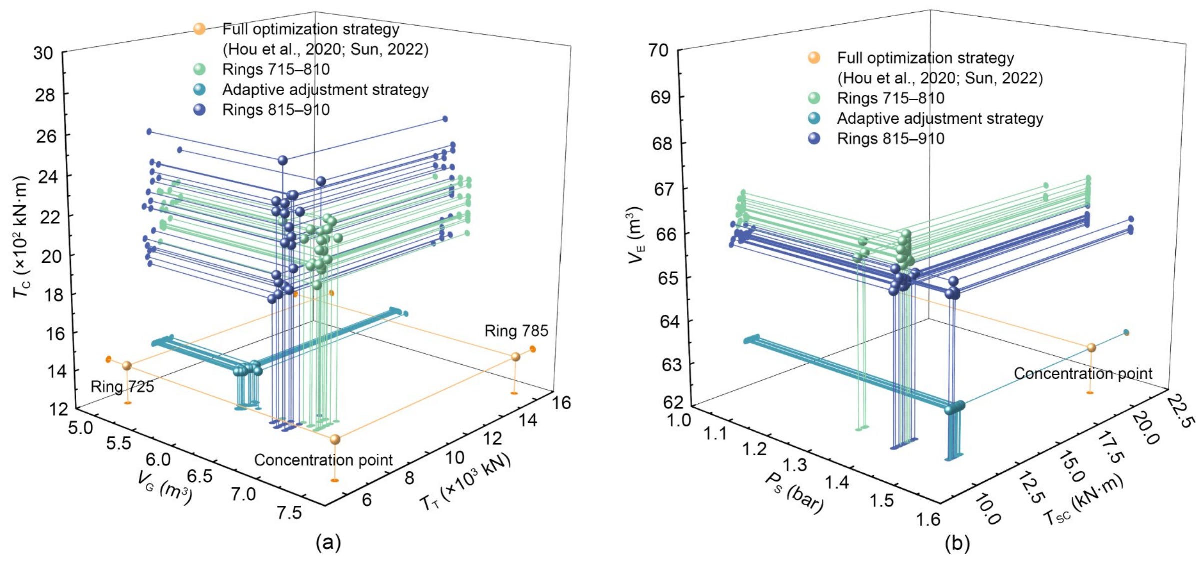

Fig. 12 Distributions of the uncontrollable parameters of Rings 715–910 in full optimization strategy and adaptive adjustment strategy: (a) T_C–V_G–T_T parameter space; (b) V_E–P_S–T_{SC} parameter space

minimum values for these two operation parameters are prominent in the initial data distribution (Fig. S12 of the ESM) and may be generated under special ground conditions. However, the test section may lack the necessary conditions to achieve extreme values, and the parameter variations in Categories B and C of the adaptive adjustment strategy further constrain the actual results for T_C and V_E. Thus, while unable to reach the theoretical minimum values, they remain very close to them.

Based on the actual monitored data, the results of the uncontrollable parameters in the full optimization strategy exhibit an average deviation of ±34.27% from the theoretical target values. The coupling effects with the ground conditions are ignored, leading to an imbalance in the matching of parameters such as P_S and T_T. In contrast, the average fluctuation in the results of uncontrollable parameters in the adaptive mechanism is only ±13.95%, and their trend of change exhibits significant synergy with the optimization direction of controllable parameters: when P_S is optimized to 1.4–1.5 bar, T_T automatically matches 8–10 MN (an improvement of 37.90% over 6.5 MN by the method proposed by Hou et al. (2020)), which aligns with the coupling effects in the geotechnical parameters and conforms to the mechanical force transmission principles of an EPB shield.

Fig. 13 shows the predicted and measured S_S in the two execution strategies of Rings 715–910. In the full optimization strategy, the predicted S_S is smaller, but the actual average increase in S_S is 1.47 mm. This is primarily because the interaction relationship constraints cause changes in the uncontrollable parameters, thereby leading to significant control errors. In contrast, the adaptive adjustment strategy achieves smaller predicted settlement errors through collaborative parameter values, with an average increase in S_S of 0.32 mm. The average measurement values of the two strategies were 4.72 and 3.81 mm, representing improvements of 23.25% and 38.05% compared to the baseline average S_S of 6.15 mm (Rings 170–665 without optimization), respectively. The latter strategy demonstrated significantly superior pre-control effects on surface settlement caused by shield tunneling compared to the former strategy.

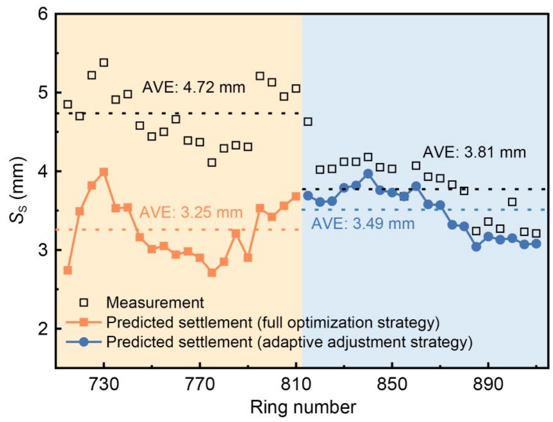

Fig. 13 S_S results for Rings 715–910. AVE is the average value

The study used a novel automation to reduce the effects of interactions between shield operation parameters and to pre-control S_S. We believe that the methodology proposed in this study will provide a versatile scientific solution for the control of surface settlement caused by shield tunneling and the refinement of operational parameters. The training dataset of the S_S prediction model was primarily based on weathered mudstone and silty clay profiles. The miscellaneous fill layer encountered at the subsequent positions of the tunnel exhibits mechanical properties that slightly deviate from the training distribution. Consequently, while the model captures the general behavioral trends in such zones, the quantitative accuracy may be lower compared to well-represented layers. In future studies, we aim to expand the training dataset to include a wider variety of anthropogenic fill layers and incorporate micromechanical indicators to enhance the model's robustness when encountering ground conditions whose mechanical properties fall outside the range represented in the training dataset.

5 Conclusions

Considering the controllability of parameters and their interactive synergies in practical shield engineering contexts, this research introduces an adjusting approach for shield operation parameters that integrates optimization and inversion. Initially, a meta-model (MHSA-Bi-LSTM) considering pre-shield arrival surface settlement is established for the real-time prediction of S_S. The parameters that are dominant regarding predicting S_S and the parameters that S_S is most sensitive to are searched using the PSO method, while the parameters that S_S is less sensitive to are predicted through inverse models, constructing a hybrid optimization mechanism by combining both. Implementing this method in practical construction facilitates the self-adaptation of the EPB shield operation and pre-control over shield tunneling-induced surface settlement. The primary conclusions are summarized as follows:

(1) During the development of Model 1 utilizing diverse methodologies, the settlement predictions made by the MHSA-Bi-LSTM model demonstrated a high degree of concordance with the empirically measured settlements, with an MAE of 0.283, RMSE of 0.352, and R^2 of 0.780. The superior predictive performance of the MHSA-Bi-LSTM model compared to the Bi-LSTM, Transformer, RF, and SVR models (Fig. S9 of the ESM) is credited to its enhanced memory retention and MHSA mechanisms, which effectively capture spatiotemporal dependencies in shield tunneling data.

(2) GSA, utilizing the Sobol' method, has demonstrated that within the nine shield operation parameters under consideration, a significant correlation exists between the surface settlement, V_E, and P_S, as well as the cutterhead parameters, including R_C and T_C, which is consistent with the theoretical study. Optimization of Category A parameters identified that within a certain range, a decrease in V_E, R_C, and T_C, along with an increase in P_S, can have a reducing effect on the surface settlement.

(3) Addressing scenarios with limited monitoring accuracy, the RF model was adapted to construct an inverse prediction model (Models 2 and 3) for parameters of Categories B and C. The results obtained using the RF model are more accurate than the results obtained using the SVR model, and the MAE and RMSE of the test set were reduced by 27.46% and 27.03% on average, respectively.

(4) During the validation of the effectiveness of the adaptive method, the predicted values of S_S for the test set were reduced to a certain extent, with an average reduction of 2.41 mm (47.55%) and an average reduction of 2.59 mm (49.28%) compared to the measured values.

(5) The adaptive adjustment strategy demonstrated significant advantages in regulating the uncontrollable parameters compared with the full optimization strategy. The full optimization strategy caused an average deviation of ±34.27% in uncontrollable parameters from theoretical targets, ignoring the coupling effects with the ground conditions and leading to imbalances in parameter matching. In contrast, the adaptive adjustment strategy restricted the average fluctuation of the uncontrollable parameters to ±13.95%, and the trend of parameter changes showed significant synergy with the optimization direction of controllable parameters.

(6) On-site verification showed that in the full optimization strategy, changes in uncontrollable parameters under interaction constraints led to significant control error. In contrast, the adaptive strategy mechanism achieved smaller prediction errors through collaborative parameters, with an average increase of only 0.32 mm in S_S. Compared with the baseline average S_S of 6.15 mm (Rings 170–665 without optimization), the average S_S values of the full optimization strategy and the adaptive adjustment strategy are 4.72 and 3.81 mm, representing improvements of 23.25% and 38.05%, respectively. This indicated that the adaptive mechanism has significantly superior pre-control effects on shield tunneling-induced surface settlement.

It should be emphasized that the factors examined in the study are among the most frequently encountered and are universally adaptable. However, the study did not touch upon specific factors required in special ground conditions (e.g., the need to consider the location and size of karst caves or the implementation of special support and reinforcement measures in soft ground), which are aspects that need to be investigated in the future.

Acknowledgments

This work is supported by the National Natural Science Foundation of China (No. 51578263) and the Jilin Provincial Department of Transport Project, China. China Railway 22 Bureau Group Track Engineering Co., Ltd. is gratefully acknowledged for generously providing the experimental platform.

Author contributions

Dongsheng WEI: writing–original draft, validation, software, methodology, investigation, and conceptualization. Haibin WEI, Lijie SUN, and Xiaokun YU: supervision. Zipeng MA and Heting WEI: writing–review & editing and supervision.

Conflict of interest

Dongsheng WEI, Haibin WEI, Zipeng MA, Heting WEI, Lijie SUN, and Xiaokun YU declare that they have no known competing financial interests or personal relationships that could have appeared to influence the work reported in this paper.

Declaration on the use of generative AI tools

No generative AI tools were used in the preparation of this manuscript.

Data availability

The data that support the findings of this study are available from the corresponding author upon reasonable request.

References

Al Mehedi MA, Amur A, Metcalf J, et al., 2023. Predicting the performance of green stormwater infrastructure using multivariate long short-term memory (LSTM) neural network. *Journal of Hydrology*, 625:130076. https://doi.org/10.1016/j.jhydrol.2023.130076

Bao WJ, Su WZ, Zhao X, et al., 2025. A study on short-term vegetable price prediction based on the CNN-LSTM-Attention model. *Discover Food*, 5(1):176. https://doi.org/10.1007/s44187-025-00426-2

Chen HY, Li XY, Feng ZB, et al., 2023. Shield attitude prediction based on Bayesian-LGBM machine learning. *Information Sciences*, 632:105-129. https://doi.org/10.1016/j.ins.2023.03.004

Chen RP, Zou N, Wu HN, et al., 2022. Review of prediction and control for surface settlement caused by shield tunneling based on machine learning. *Journal of Huazhong University of Science and Technology (Natural Science Edition)*, 50(8):56-65 (in Chinese). https://doi.org/10.13245/j.hust.220806

Cheng JCP, Lu QQ, Deng YC, 2016. Analytical review and evaluation of civil information modeling. *Automation in Construction*, 67:31-47. https://doi.org/10.1016/j.autcon.2016.02.006

Cheng XS, Zhang SL, Zhou XH, et al., 2022. Parameter analysis of excavation face stability of shield tunnel under high water pressure seepage. *Physics and Chemistry of the Earth, Parts A/B/C*, 128:103218. https://doi.org/10.1016/j.pce.2022.103218

Deng XH, Wang BL, 2013. Analysis of influence of shield tunneling crossing underneath intercity railway and shield tunneling parameters optimization. *Applied Mechanics and Materials*, 353-356:1619-1624. https://doi.org/10.4028/www.scientific.net/AMM.353-356.1619

Dige N, Diwekar U, 2018. Efficient sampling algorithm for large-scale optimization under uncertainty problems. *Computers & Chemical Engineering*, 115:431-454. https://doi.org/10.1016/j.compchemeng.2018.05.007

Ding LY, Wang F, Luo HB, et al., 2013. Feedforward analysis for shield-ground system. *Journal of Computing in Civil Engineering*, 27(3):231-242. https://doi.org/10.1061/(ASCE)CP.1943-5487.0000219

Dong M, Guan MZ, Wang KH, et al., 2025. Machine learning-based measurement and prediction of ground settlement induced by shield tunneling undercrossing existing tunnels in composite strata. *Sensors*, 25(5):1600. https://doi.org/10.3390/s25051600

Galera JM, Pescador S, Rodríguez Á, et al., 2007. Prediction of the ground conditions ahead the TBM face in the tunnels of guadarrama (Spain), using geophysical methods and in situ testing. ITA-AITES World Tunnel Congress–Underground Space–the 4th Dimension of Metropolises, p.203-208. https://doi.org/10.1201/noe0415408073.ch33

Gao MT, Yang WF, Liu ZY, et al., 2024. LSTM goaf surface subsidence prediction method combining convolutional neural network and attention mechanism. *Bulletin of Surveying and Mapping*, (6):53-58 (in Chinese). https://doi.org/10.13474/j.cnki.11-2246.2024.0610

Ghaboussi J, Ranken RE, 1977. Interaction between two parallel tunnels. *International Journal for Numerical and Analytical Methods in Geomechanics*, 1(1):75-103. https://doi.org/10.1002/nag.1610010107

Hage Chehade F, Shahrour I, 2008. Numerical analysis of the interaction between twin-tunnels: influence of the relative position and construction procedure. *Tunnelling and Underground Space Technology*, 23(2):210-214. https://doi.org/10.1016/j.tust.2007.03.004

Herrenknecht AG, 2024. Pioneering Underground Together. Herrenknecht AG. https://www.herrenknecht.com/en

Hia S, Kuswanto H, Prastyo DD, 2023. Robustness of support vector regression and random forest models: a simulation study. *In*: Wah YB, Berry MW, Mohamed A, et al. (Eds.), Data Science and Emerging Technologies. Springer, Singapore, p.465-479. https://doi.org/10.1007/978-981-99-0741-0_33

Hou GY, Xu ZD, Li L, et al., 2020. Shield tunneling parameter matching model and UI interface. *Advances in Civil Engineering*, 2020:9562828. https://doi.org/10.1155/2020/9562828

Hou YJ, Zhou MZ, Zhang DL, et al., 2022. Analysis of four shield-driven tunnels with complex spatial relations in a clay stratum. *Tunnelling and Underground Space Technology*, 124:104478. https://doi.org/10.1016/j.tust.2022.104478

Hu AF, Wang C, Xie SL, et al., 2025. Machine learning for soil parameter inversion enhanced with Bayesian optimization. *Journal of Zhejiang University-SCIENCE A*, 26(11):1034-1051. https://doi.org/10.1631/jzus.A2400568

Hu XY, Cheng JG, Ju JW, 2021. Influence of the cutterhead configuration and operation parameters on the face stability of EPB shield tunnels in dry granular soils. *International Journal of Geomechanics*, 21(5):04021050. https://doi.org/10.1061/(ASCE)GM.1943-5622.0002008

Huang HW, Chang JQ, Zhang DM, et al., 2022. Machine learning-based automatic control of tunneling posture of shield machine. *Journal of Rock Mechanics and Geotechnical Engineering*, 14(4):1153-1164. https://doi.org/10.1016/j.jrmge.2022.06.001

Huang K, Sun YW, Zhou DQ, et al., 2021. Influence of water-rich tunnel by shield tunneling on existing bridge pile foundation in layered soils. *Journal of Central South University*, 28(8):2574-2588.

https://doi.org/10.1007/s11771-021-4787-6

Kim CY, Bae GJ, Hong SW, et al., 2001. Neural network based prediction of ground surface settlements due to tunnelling. *Computers and Geotechnics*, 28(6-7):517-547. https://doi.org/10.1016/S0266-352x(01)00011-8

Kong FC, Lu DC, Ma YD, et al., 2022. Analysis and intelligent prediction for displacement of stratum and tunnel lining by shield tunnel excavation in complex geological conditions: a case study. *IEEE Transactions on Intelligent Transportation Systems*, 23(11):22206-22216. https://doi.org/10.1109/Tits.2022.3149819

Li C, Li JH, Shi ZQ, et al., 2022. Prediction of surface settlement induced by large-diameter shield tunneling based on machine-learning algorithms. *Geofluids*, 2022:4174768. https://doi.org/10.1155/2022/4174768

Li JH, Li PX, Guo D, et al., 2021. Advanced prediction of tunnel boring machine performance based on big data. *Geoscience Frontiers*, 12(1):331-338. https://doi.org/10.1016/j.gsf.2020.02.011

Li JP, Huang HX, Wang G, 2025. A small-sample prediction model for ground surface settlement in shield tunneling based on adjacent-ring graph convolutional networks (GCN-SSPM). *Buildings*, 15(19):3519. https://doi.org/10.3390/buildings15193519

Li ZC, Chen RP, Meng FY, et al., 2015. Tunnel boring machine tunneling-induced ground settlements in soft clay and influence of excavation parameters. *Journal of Zhejiang University (Engineering Science)*, 49(7):1268-1275 (in Chinese). https://doi.org/10.3785/j.issn.1008-973X.2015.07.010

Lin CJ, Yang XD, Gong YJ, et al., 2021. Prediction model of in-chamber earth pressure for EPB shield based on PSO-BP and parameter sensitivity analysis of tunneling parameters. *Journal of Basic Science and Engineering*, 29(5): 1220-1233 (in Chinese). https://doi.org/10.16058/j.issn.1005-0930.2021.05.011

Liu WL, Ding LY, 2020. Global sensitivity analysis of influential parameters for excavation stability of metro tunnel. *Automation in Construction*, 113:103080. https://doi.org/10.1016/j.autcon.2020.103080

Luo ZJ, Li Z, Tan JZ, et al., 2020. Three-dimensional fluid–soil full coupling numerical simulation of ground settlement caused by shield tunnelling. *European Journal of Environmental and Civil Engineering*, 24(8):1261-1275. https://doi.org/10.1080/19648189.2018.1464961

Lv JB, Li XL, Fu HL, et al., 2020. Influence of shield tunnel construction on ground surface settlement under the condition of upper-soft and lower-hard composite strata. *Journal of Vibroengineering*, 22(5):1126-1144. https://doi.org/10.21595/jve.2020.20967

Mair RJ, Taylor RN, Bracegirdle A, 1993. Subsurface settlement profiles above tunnels in clays. *Géotechnique*, 43(2): 315-320. https://doi.org/10.1680/geot.1993.43.2.315

Maleki MR, 2018. Rock joint rate (RJR): a new method for performance prediction of tunnel boring machines (TBMs) in hard rocks. *Tunnelling and Underground Space Technology*, 73:261-286. https://doi.org/10.1016/j.tust.2017.12.022

MOHURD (Ministry of Housing and Urban-Rural Development of the People's Republic of China), SAMR (State Administration for Market Regulation of the People's Republic of China), 2019. Standard for Geotechnical Testing Method, GB/T 50123-2019. National Standards of the People's Republic of China (in Chinese).

Niu YL, Ren TL, Zhou Q, et al., 2023. Analysis of excavation parameters on face stability in small curvature shield tunnels. *Sustainability*, 15(8):6797. https://doi.org/10.3390/su15086797

Pourtaghi A, Lotfollahi-Yaghin MA, 2012. Wavenet ability assessment in comparison to ANN for predicting the maximum surface settlement caused by tunneling. *Tunnelling and Underground Space Technology*, 28:257-271. https://doi.org/10.1016/j.tust.2011.11.008

Rashid TA, Fattah P, Awla DK, 2018. Using accuracy measure for improving the training of LSTM with metaheuristic algorithms. *Procedia Computer Science*, 140:324-333. https://doi.org/10.1016/j.procs.2018.10.307

Richa T, Lebdaoui S, Pereira JM, et al., 2023. A comparative study of ensemble methods for prediction of surface settlement induced by TBM tunneling. Geo-Risk 2023: Innovation in Data and Analysis Methods, p.211-219. https://doi.org/10.1061/9780784484975.023

Shen ZW, Yang HZ, Zhang SJ, 2021. Neural network approximation: three hidden layers are enough. *Neural Networks*, 141:160-173. https://doi.org/10.1016/j.neunet.2021.04.011

Shi G, Qin CJ, Tao JF, et al., 2021. A VMD-EWT-LSTM-based multi-step prediction approach for shield tunneling machine cutterhead torque. *Knowledge-Based Systems*, 228:107213. https://doi.org/10.1016/j.knosys.2021.107213

Sobol' IM, 2001. Global sensitivity indices for nonlinear mathematical models and their Monte Carlo estimates. *Mathematics and Computers in Simulation*, 55(1-3):271-280. https://doi.org/10.1016/S0378-4754(00)00270-6

Song MY, Yang MH, Yao GZ, et al., 2024. Artificial intelligence driven tunneling-induced surface settlement prediction. *Automation in Construction*, 168:105819. https://doi.org/10.1016/j.autcon.2024.105819

Standing JR, Burland JB, 2006. Unexpected tunnelling volume losses in the Westminster area, London. *Géotechnique*, 56(1):11-26. https://doi.org/10.1680/geot.2006.56.1.11

Sun SL, 2022. Shield tunneling parameters matching based on support vector machine and improved particle swarm optimization. *Scientific Programming*, 2022:6782947. https://doi.org/10.1155/2022/6782947

Suwansawat S, Einstein HH, 2006. Artificial neural networks

for predicting the maximum surface settlement caused by EPB shield tunneling. *Tunnelling and Underground Space Technology*, 21(2):133-150.
https://doi.org/10.1016/j.tust.2005.06.007

Taylor KE, 2001. Summarizing multiple aspects of model performance in a single diagram. *Journal of Geophysical Research: Atmospheres*, 106(D7):7183-7192.
https://doi.org/10.1029/2000jd900719

Tsai MY, Cho HH, 2021. Differential-evolution-based weights fine tuning mechanism for GRU to predict 5G traffic flow. International Symposium on Intelligent Signal Processing and Communication Systems (ISPACS), p.1-2.
https://doi.org/10.1109/ISPACS51563.2021.9650923

Wang L, Pan QJ, Wang SY, 2024. Data-driven predictions of shield attitudes using Bayesian machine learning. *Computers and Geotechnics*, 166:106002.
https://doi.org/10.1016/j.compgeo.2023.106002

Wang LY, Que HB, Wu F, 2025. The CNN-LSTM-Attention model for short term prediction of the polar motion. *Measurement Science and Technology*, 36(1):016323.
https://doi.org/10.1088/1361-6501/ad8be5

Wang RH, Li DQ, Chen EJ, et al., 2021. Dynamic prediction of mechanized shield tunneling performance. *Automation in Construction*, 132:103958.
https://doi.org/10.1016/j.autcon.2021.103958

Wei HB, Wei DS, Jiang BY, et al., 2023. Prediction analysis of settlement of existing road under shield tunneling based on IPSO-SVR. *Journal of South China University of Technology (Natural Science Edition)*, 51(6):62-71 (in Chinese).
https://doi.org/10.12141/j.issn.1000-565X.220553

Wu B, Xu J, Huang W, et al., 2019. Prediction of ground settlement on shielded water-rich sand layer considering groundwater level and tunnel depth. *IOP Conference Series: Earth and Environmental Science*, 358(4):042045.
https://doi.org/10.1088/1755-1315/358/4/042045

Xu YJ, Chen XS, 2023. Current situation and prospect of comprehensive development of underground space in metro area. *Chinese Journal of Underground Space and Engineering*, 19(1):1-12 (in Chinese).
https://doi.org/10.20174/j.juse.2023.01.001

Yang MH, Song MY, Guo YW, et al., 2025. Prediction of shield tunneling-induced ground settlement using LSTM architecture enhanced by multi-head self-attention mechanism. *Tunnelling and Underground Space Technology*, 161:106536.
https://doi.org/10.1016/j.tust.2025.106536

Ye XW, Zhang XL, Zhang HQ, et al., 2023. Prediction of lining upward movement during shield tunneling using machine learning algorithms and field monitoring data. *Transportation Geotechnics*, 41:101002.
https://doi.org/10.1016/j.trgeo.2023.101002

Zhang N, Zhang N, Zheng Q, et al., 2022. Real-time prediction of shield moving trajectory during tunnelling using GRU deep neural network. *Acta Geotechnica*, 17(4):1167-1182.
https://doi.org/10.1007/s11440-021-01319-1

Zhang P, Chen RP, Wu HN, 2019. Real-time analysis and regulation of EPB shield steering using random forest. *Automation in Construction*, 106:102860.
https://doi.org/10.1016/j.autcon.2019.102860

Zhang P, Chen RP, Wu HN, et al., 2020a. Ground settlement induced by tunneling crossing interface of water-bearing mixed ground: a lesson from Changsha, China. *Tunnelling and Underground Space Technology*, 96:103224.
https://doi.org/10.1016/j.tust.2019.103224

Zhang P, Wu HN, Chen RP, et al., 2020b. A critical evaluation of machine learning and deep learning in shield-ground interaction prediction. *Tunnelling and Underground Space Technology*, 106:103593.
https://doi.org/10.1016/j.tust.2020.103593

Zhang P, Yin ZY, Jin YF, et al., 2020c. A novel hybrid surrogate intelligent model for creep index prediction based on particle swarm optimization and random forest. *Engineering Geology*, 265:105328.
https://doi.org/10.1016/j.enggeo.2019.105328

Zhang WG, Li HR, Wu CZ, et al., 2021. Soft computing approach for prediction of surface settlement induced by earth pressure balance shield tunneling. *Underground Space*, 6(4):353-363.
https://doi.org/10.1016/j.undsp.2019.12.003

Zhang YQ, Cao WG, Zhou SH, et al., 2021. Prediction of three-dimensional subface and subsurface settlement caused by shield tunnelling based on Peck formula. *Journal of Railway Science and Engineering*, 18(1):153-161 (in Chinese).
https://doi.org/10.19713/j.cnki.43-1423/u.T20200181

Zhao J, Yang WC, Zhu F, 2024. A CNN-LSTM-Attention model for near-crash event identification on mountainous roads. *Applied Sciences*, 14(11):4934.
https://doi.org/10.3390/app14114934

Zhou XZ, Zhao C, Bian XC, 2023. Prediction of maximum ground surface settlement induced by shield tunneling using XGBoost algorithm with golden-sine seagull optimization. *Computers and Geotechnics*, 154:105156.
https://doi.org/10.1016/j.compgeo.2022.105156

Zhou Z, Zhang JJ, Ding HH, et al., 2023. Settlement prediction model of shield tunnel under-crossing existing tunnel based on GA-Bi-LSTM. *Chinese Journal of Rock Mechanics and Engineering*, 42(1):224-234 (in Chinese).
https://doi.org/10.13722/j.cnki.jrme.2021.1187

Electronic supplementary materials

Sections S1–S5, Tables S1 and S2, Figs. S1–S12